

Supplementary Information for “High-throughput microscopy to determine morphology, microrheology, and phase boundaries applied to phase separating coacervates”

Yimin Luo, Mengyang Gu, Chelsea E.R. Edwards,
Megan T. Valentine, Matthew E. Helgeson

March 14, 2022

Note 1 Colloid addition

Note 1.1 Colloid partitioning based on surface chemistry

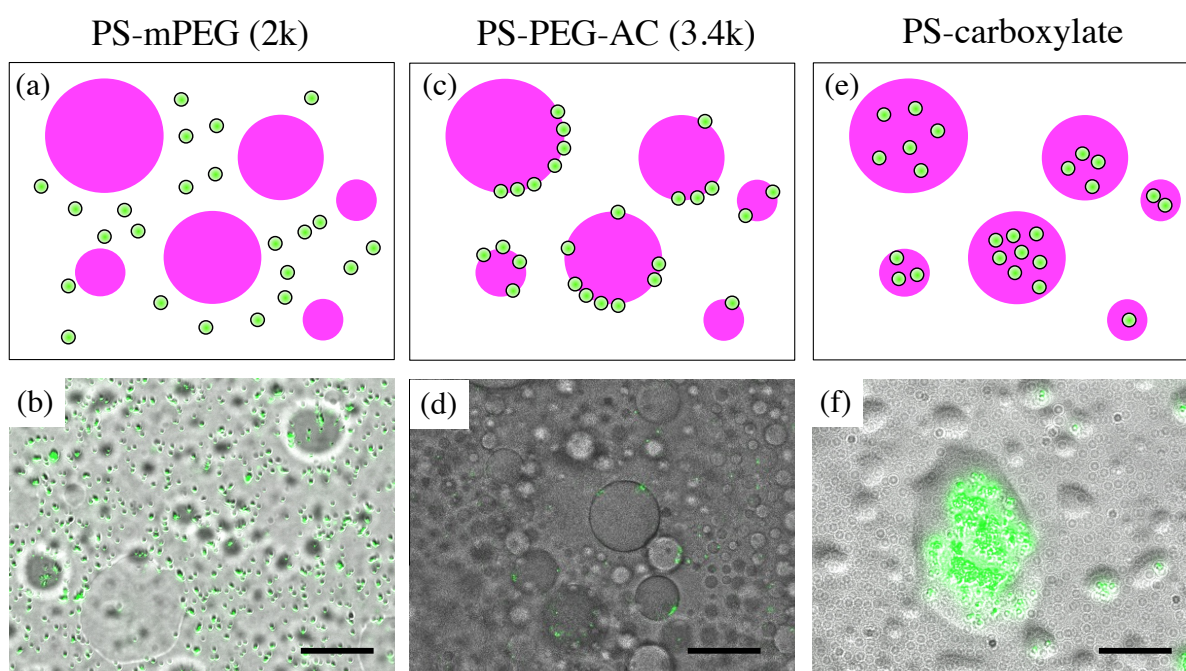


Figure S1: Preferential partitioning of colloids of three different surface chemistries. Panels (a,c,e) show sketches of the localization where the PEC phase is denoted by magenta, the colloids by green, and the dilute phase by the white background. Panels (b,d,f) show the corresponding merged bright field channel, which shows the PEC phase, and fluorescent channel that shows fluorescently-labeled colloids. The scale bars are 100 μm .

Note 1.2 Charge introduced by adding carboxylate particles to the PEC phase

Given that the probe particle used has a zeta potential of about $Z = -37$ mV, the surface charge density is computed using the Grahame equation [4]:

$$\sigma = \sqrt{8\epsilon_0\epsilon k_B T} \sinh\left(\frac{eZ}{2k_B T}\right) \quad (1)$$

where e is charge of an electron, ϵ_0 and ϵ are the permittivity of the free space and relative permittivity of the medium, k_B is the Boltzmann constant, and T denotes the absolute temperature. At 25 °C, $\epsilon = 50$ at 3M of salt, the surface charge is estimated to be $\sigma = -0.1588$ C/m². In addition, the particle concentration is 0.01%, which corresponds to a number density of 1.9×10^7 particles/mL. As a result, the number of charges contributed to the PEC by the carboxylate particles is estimated to be about 9.5×10^{-6} C/mL, or about 10^{-10} mol ions/mL. Given that the added salt concentration is typically in the range of 3-4.5M, this corresponds to around $3-4.5 \times 10^{-3}$ mol ions/mL. Thus, the amount of charge introduced by the carboxylate particles is negligible in these systems and can be ignored.

Note 2 Benchmark microrheology measurements

Note 2.1 Characterizing the noise floor

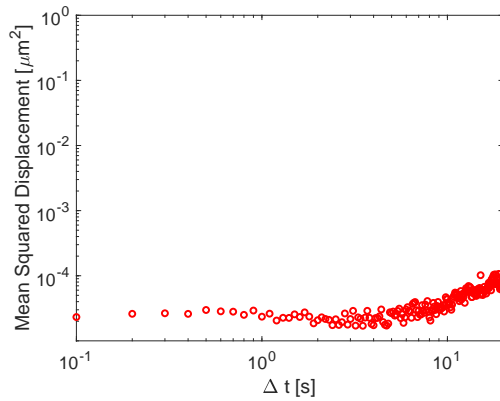


Figure S2: Measuring the apparent MSD of particles that are similar to those used in the experiments but are immobilized in a crosslinked polymer matrix. The low-frequency plateau value provides an estimate of the static noise floor.

Note 2.2 Varying processing conditions

At many compositions, certain flow mixing conditions result in the appearance of droplet-aggregate morphologies in the PAH-PAA-NaCl system, which are often associated with kinetically arrested so-called “precipitates” [2]. We aimed to verify that our samples, which settled and equilibrated for several days under gravity, produced similar viscosity as compared to samples of identical initial composition measured immediately after centrifugation. We found excellent agreement between the results obtained by the two processing methods when the particle MSDs calculated using MPT were compared at 100 mM total repeat units and 4.5 M NaCl (Fig. S3). We suspect that this is because aggregate morphologies generally do not form at the high ionic strength conditions tested in this work.

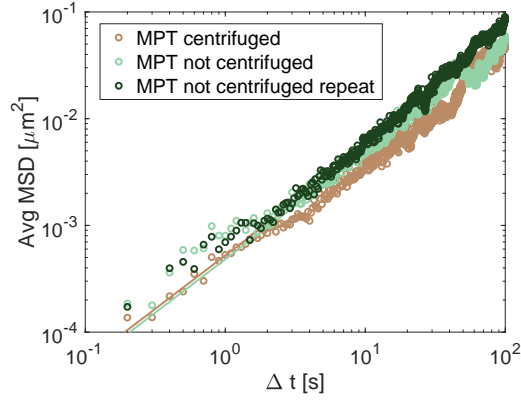


Figure S3: Comparison of MSDs of centrifuged and not centrifuged samples, prepared from initial composition $\phi_0 = 100$ mM total repeat units and $\psi_0 = 4.5$ M

Note 2.3 Sampling bias detection

To determine whether sampling bias was present, we compiled MSDs from four different videos of the same sample composition at $C_p = 100$ mM, $C_s = 4.5$ M (Fig. S4) and found reproducible MSD values in all cases.

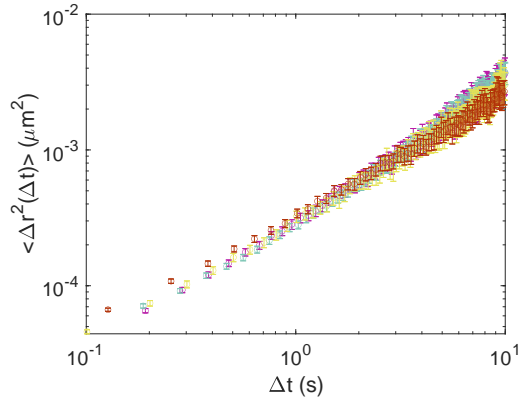


Figure S4: Reproducibility of microrheology verified by comparing the results obtained at four different locations in the sample.

Note 2.4 Sample particle displacements at different z-planes

To determine whether concentration gradient exists, we sampled the MSD from three different planes (Fig. S5) in an equilibrated sample, and detected no significant difference among them.

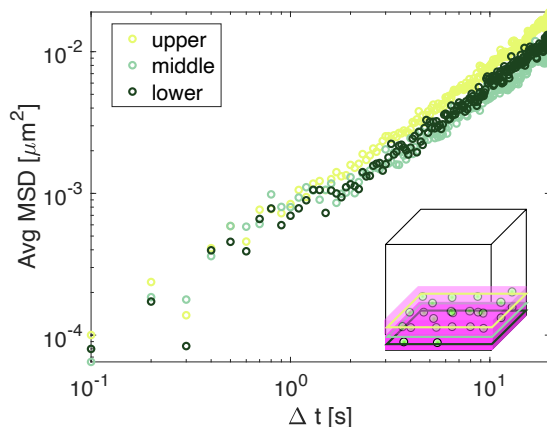


Figure S5: Comparison of MSDs in three different depth planes in a sample 5 days after demixing. The color of the symbols match the corresponding layers as illustrated in the schematics. These MSDs were acquired using a different microscope (Olympus IX73), hence the slightly larger noise at low Δt .

Note 2.5 Extraction of zero-shear viscosity from MSD

Truncating larger Δt for MSD analysis is customarily done for microrheology studies [3], as MSD at large Δt suffers from poor statistics due to the small number of trajectories that exist to calculate their averages. A typical MSD plot with standard deviation for all Δt 's is shown in Fig. S6. Beyond 20% Δt the error in MSD begin to increase dramatically.

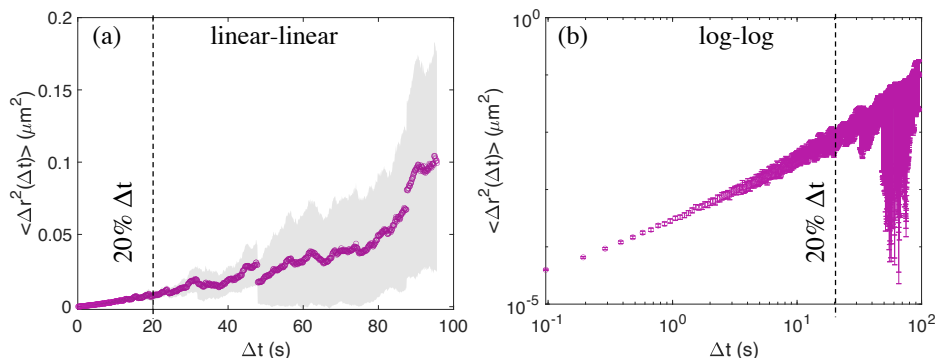


Figure S6: MSD of of a reference sample ($C_p = 100$ mM, $C_s = 4.5$ M) plotted in (a) linear-linear and (b) log-log plots where dashed lines denote location of 20% Δt .

We used a weighted fitting routine that included a weight factor in the calculation of the regression statistic, with weighting that is inversely proportional to the standard deviation of the MSD value at each Δt . Because the standard deviation increases as the number of independent data points used to calculate the MSD decreases for long values of Δt (grey region on the left plot, error bars on the right plot), these values will naturally contribute less to the best-fit viscosity. This was confirmed by performing an additional sensitivity analysis where the longest lag time used in the analysis was varied from 10%-50% of the longest Δt . The analysis is summarized below in Table S1, and shows that using more than 20% of the longest Δt provides identical estimates of the viscosity to within 3%.

Note 3 Bulk rheometry

To ensure that the viscosity measured by microrheology is robust and comparable to previous studies using bulk rheometry, we performed a number of benchmarking experiments for one initial composition at $C_p = 100$ mM (= 50 mM PAA + 50 mM PAH, inclusive of counter-ions), and $C_s = 4.5$ M in added salt.

Table S1: Sensitivity analysis for fitting the MSD

Δt selected	η_0^* (Pa·s)	Interval
10%	6.3276	[6.2538, 6.4032]
20%	6.2329	[6.1641, 6.3033]
30%	6.1370	[6.0721, 6.2032]
40%	6.0916	[6.0282, 6.1562]
50%	6.0374	[5.9757, 6.1003]

The PEC-dense phase that results from this initial composition has polymer concentration and viscosity values that lie roughly in the middle of the range of values across all samples measured in this study.

The reference bulk rheology value was measured by making an identical sample to that used in experiments but without tracer particles added. The polyelectrolytes were mixed with a stock salt solution, with total volume of 10 mL, and centrifuged at 2000 rpm for 30 minutes until complete phase separation was achieved. The supernatant was removed and the PEC was loaded onto an AR-G2 stress-controlled rheometer (TA Instruments, New Castle, DE). We performed a frequency-sweep in the linear viscoelastic limit using a 25-mm diameter parallel plate fixture, at 2% shear strain over a frequency range of 0.01 - 10 rad/s. The instrument is outfitted with a solvent trap, and a home-made moisture chamber to minimize evaporation during testing. The resulting measured viscosity of the dense phase is ~ 5 Pa s. Although this exhibits some quantitative discrepancy from the viscosity measured by microrheology (~ 8 Pa s), this difference is comparable to other studies in which agreement between microrheology and bulk rheology measurements was observed [6].

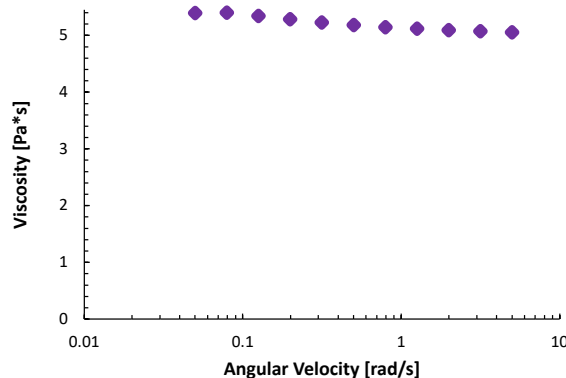


Figure S7: Complex viscosity obtained by bulk rheology, prepared from initial composition $C_p = 100$ mM total repeat units and $C_s = 4.5$ M.

Note 4 Verification of the composition of the stock solution

To ensure the accuracy of the initial composition and to establish control, we apply the same TGA protocol used to determine the composition of PEC-rich phase to examine the composition of stock solutions prepared at 1M and 2M. In Table S2, the column 2 and 3 show the theoretical wt% of each mixture, calculated with or without counter-ions, respectively. After determining the water wt% after dehydration at 110 °C for 2h, the dried mixture is heated at 600 °C for 12h. Column 4 and 5 show the wt% of the total mixture that remains or is burned off after this step. In determining the PEC-rich phase composition, it is generally assumed that the polymer complex is completely burned off and that only the NaCl remains. In the case of unpaired ions, such as with the stock solution, Table S2 illustrates that, in the case of PAH, column 5 roughly matches column 2, indicate that the HCl in PAH completely evaporates. However, comparing the first 3 columns indicate that, the wt% remains (column 4) after burning at 600 °C exceeds the wt% of Na+ originally present in the stock solution (the difference between column 1 and 2). We reconcile this by recognizing that Na (MW = 23 g/mol) reacts with carbon to form Na₂CO₃ (MW = 106 g/mol), in this process. A mass balance of the element Na quickly confirms

Table S2: TGA measurements of the composition (in wt%) of the stock solution

Sample description	calculated polymer wt%		wt% before & after heating at 600 °C	
	w/ counter-ion	w/o counter-ion	remained	burned off
PAA-Na (15k, 2M)	16.98	13.01	9.73±0.09	7.4±0.16
PAH (17.5k, 2M)	18.56	11.38	0.4±0.24	17.34±0.58
PAA-Na (15k, 1M)	8.92	6.84	5.39±0.13	3.86±0.04
PAH (17.5k, 1M)	9.30	5.70	0.42±0.30	8.75±0.09

the accurate composition of the stock solution ($\text{wt\% remain} = \frac{16.98\% - 13.01\%}{23\text{g/mol}} \frac{106\text{g/mol}}{2} = 9.14\%$). This measurement serves as a control to help us interpret the TGA results of the PEC-rich phase composition, in addition to allowing us accurate placement of the initial compositions on the phase diagram.

Note 5 Stages of phase separation

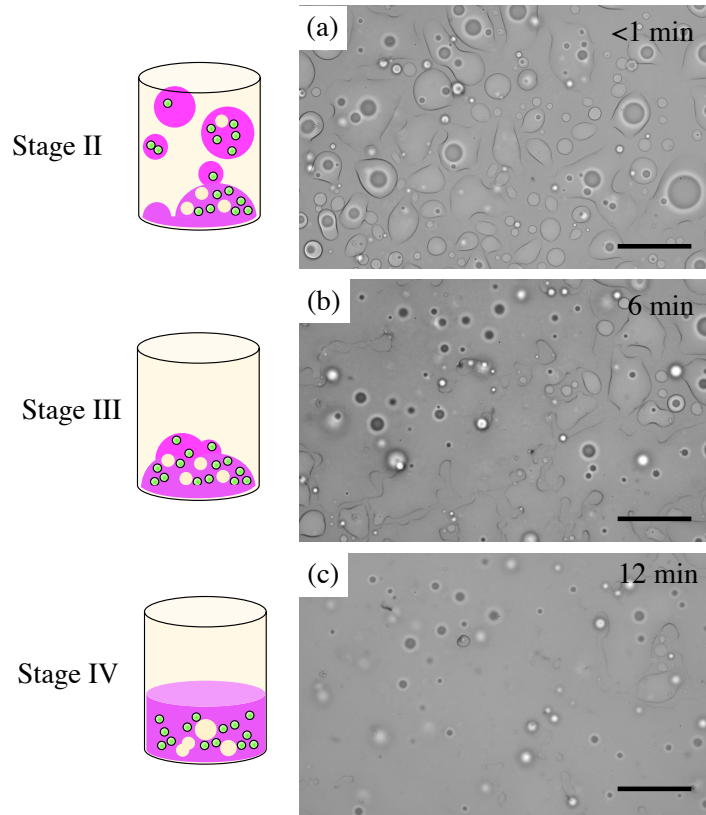


Figure S8: The phase separation occurs in four stages, in a sample with $(C_p, C_s) = (100\text{mM}, 4.5\text{M})$. Stage I: nucleation of the droplets. This stage occurs rapidly and is not observed. (a) Stage II: Droplet sedimentation: most of the droplets are suspended in the bulk and the sample appears very turbid; turbidity measurements are commonly used to characterize the extent of complex formation during this step. (b) Stage III: External coalescence: the bulk is free of droplets, droplets sitting on the bottom inter-diffuse to merge into one continuous phase. (c) Stage IV: Internal coalescence: the dense phase contains droplets of dilute phase, because the continuous dense phase is highly viscous, the inner structure continues to coarsen. The scale bar is $100\ \mu\text{m}$.

Note 6 Curve fitting procedure and error propagation analysis

Note 6.1 Least square fit to find degree of ionization α from tie lines

The stock polyelectrolyte solution contains not only the polyelectrolyte but also the associated counter-ions, which account for significant weight fraction of the complexes, as verified by TGA analysis (Table S1). Furthermore, the counter-ions in the polyelectrolytes combine to form NaCl, and contribute to the total salt concentration, along with the added salt.

Consider a set of composition state point pairs $\{C'_p, C'_s | C_p^*, C_s^*\}$ that define the tie lines between them on a boundary in between dilute and dense phase (Figure S9a). Experimentally, we can approximate these state points by TGA measurement replicates. Conservation of mass in a fixed volume requires that the tie lines be linear, such that the entire tie line can be described by:

$$C_{s,0} = C'_s + \frac{C_s^* - C'_s}{C_p^* - C'_p} (C_{p,0} - C'_p) \quad (2)$$

where $(C_{p,0}, C_{s,0})$ is a point on the tie line within the phase boundary and also stands for the initial composition before phase separation. Rearranging Eq.2 produces the following:

$$\frac{C_{s,0} - C'_s}{C_s^* - C'_s} = \frac{C_{p,0} - C'_p}{C_p^* - C'_p} \quad (3)$$

Hence, from the above expression, all points on the tie line, after transformation, will fall on a straight line passing through (0,0) and (1,1) (Fig. S9b), and can be used to construct a global fitting for the initial composition:

$$\begin{aligned} C_{p,0} &= C_p \\ C_{s,0} &= C_s + \alpha \cdot C_p \end{aligned}$$

Thus, the total salt in the initial mixture depends on α . We then minimize the the mean-squared error (MSE), which is the shortest distance between observed $(\frac{C_{p,0} - C'_p}{C_p^* - C'_p}, \frac{C_{s,0} - C'_s}{C_s^* - C'_s})$ and the theoretical line passing through (0,0) and (1,1). The variation in MSE with changing α is plotted below, and we find that the MSE is minimized when $\alpha = 0.13$ (Fig.S9c).

We assume that α is insensitive to the range of salt and polymer concentrations considered. The optimal solution, $\alpha = 0.13$, results in a distribution of initial compositions around the tie line as shown by the filled red circles (Fig. S9d). Since $\alpha \ll 1$, this analysis is necessary for accurately mapping the phase diagram at concentrations near the critical point.

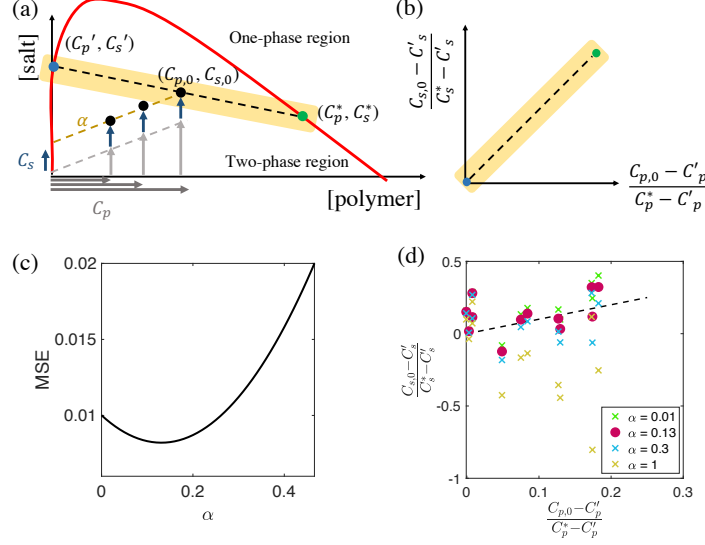


Figure S9: (a) Schematic diagram illustrating an exemplar case of constant added salt (deep blue arrows) and varying added complex (grey arrows) on polymer and salt molar concentration phase diagram. The red solid line denotes the binodal phase boundary. The dilute and dense phase state points are denoted by blue and green filled circles, and the tie line between them is denoted by the black dashed line. The yellow shaded box highlights a single tie line before transformation. (b) After transformation, all tie lines can be expressed as a single one passing through (0,0) and (1,1). (c) The mean-squared error (MSE), defined as the shortest distance between the initial composition for α , and the tie lines determined by the state points. (d) Experimental determination of the degree of polyelectrolyte ionization, α . Different colors show estimates for the different initial concentrations for a given value of α , along with the dashed tie lines renormalized to pass through (0,0) and (1,1). The points corresponding to the error-minimizing value of α are denoted by \bullet 's while the rest are denoted by \times 's.

Note 6.2 Different model fitting for PEC-rich phase composition to the zero-shear viscosity

Based on these observations, we consider three models for scaling of the viscosity: (1) Model 1: where the viscosity only depends on polymer concentration, $\eta_0^* = \eta_0^*(\phi^*|\psi^*)$, (2) Model 2: where the viscosity only depends on salt concentration, $\eta_0^* = \eta_0^*(\psi^*|\phi^*)$ and (3) Model 3: where the viscosity depends both on polymer and salt concentration, $\eta_0^* = \eta_0^*(\phi^*, \psi^*)$. The intent of simultaneously investigating these three independent models is to determine whether model (3) provides a statistically distinguishable better fit to the data, and therefore a significant cross-dependence of the salt concentration on the scaling with respect to polymer concentration, and vice versa. These Models are first recapitulated here from the main text to find their linearized form:

$$\begin{aligned} \text{Model 1 : } \eta_0^*(\phi^*) &= C_1(\phi^*)^\beta & (4) \\ \Rightarrow \log(\eta_0^*) &= \log(C_1) + \beta \log(\phi^*). & (5) \end{aligned}$$

We assume that in the range of ϕ^* probed, C_1 is insensitive to ψ^* and is therefore assumed to be constant.

$$\text{Model 2 : } \eta_0^*(\psi^*) = C_2 \exp(-a(T)\sqrt{C_s^*}) = C_2 \exp(-A\sqrt{\psi^*}) \quad (6)$$

$$\Rightarrow \log(\eta_0^*) = \log(C_2) - A\sqrt{\psi^*} \quad (7)$$

Similar to Model 1, we again assume that in the range of ψ^* probed, C_2 is insensitive to ϕ^* and is therefore assumed to be constant. Linearization and fitting of the model is used to find the dependence between $\log(\eta_0^*)$ and $\sqrt{\psi^*}$.

$$\text{Model 3 : } \eta_0^*(\phi^*, \psi^*) = C_3(\phi^*)^{\tilde{\beta}} \exp(-\tilde{A}\sqrt{\psi^*}) \quad (8)$$

$$\Rightarrow \log(\eta_0^*) = \log(C_3) + \tilde{\beta} \log(\phi^*) - \tilde{A}\sqrt{\psi^*}, \quad (9)$$

where the coefficient C_3 now reflects the potential combined dependence of C_1 on the salt concentration ψ^* and C_2 on the polymer concentration ϕ^* .

Note 6.3 Reconstructing the phase boundary $\psi^*(\phi^*)$ and uncertainty quantification

We separately fit linear regression models for zero-shear viscosity with respect to polymer concentrations and salt concentrations in the binodal boundary

$$\eta_0^* = \log(C_1) + \beta \log(\phi^*) + \epsilon_1 \quad (10)$$

$$\eta_0^* = \log(C_2) - A\sqrt{\psi^*} + \epsilon_2 \quad (11)$$

where $\epsilon_1 \sim N(0, \sigma_1^2)$ and $\epsilon_2 \sim N(0, \sigma_2^2)$ are both independent Gaussian noise. Note that the measurement error in the covariates (here, ϕ^* and ψ^*) was not considered in the linear regression model. Here since the measurement error is much smaller than the range of the covariate, the bias is small.

We follow a Bayesian approach by assuming objective priors $\pi(\log C_1, \beta, \sigma_1^2)1/\sigma_1^2$ and $\pi(\log C_2, A, \sigma_2^2) \propto 1/\sigma_2^2$ [1]. The posterior distribution of $p((\log C_1, \beta) | \phi^*, \eta_0^*)$ and $p((\log C_2, A) | \psi^*, \eta_0^*)$ both follow a noncentral Student's t distribution with $n-2$ degrees of freedom.

Since the signal in the linear regression model by two regression models

$$\log(C_1) + \beta \log(\phi^*) = \log(C_2) - A\sqrt{\psi^*} \quad (12)$$

we have

$$\psi^* = \frac{(\log C_1 + \beta \log(\phi^*) - \log C_2)^2}{A^2}. \quad (13)$$

We then sample the parameters $(\log C_1, \beta)$ and $(\log C_2, A)$ from the posterior distributions $p((\log C_1, \beta) | \phi^*, \eta_0^*)$ and $p((\log C_2, A) | \psi^*, \eta_0^*)$, respectively. For each polymer concentrations, we obtain the posterior samples of salt concentration ψ^* , from which we can compute the 95% credible interval of the mean of the binodal boundary.

Note 6.4 Out-of-sample testing

The fitting procedure η_0^* vs ϕ^* and η_0^* vs ψ^* are tested by an out-of-sample prediction test. The data are randomly divided into a training set (open circles) and a test set (filled circles). The training set is fit to the linear model. The η_0^* value is withheld and predicted by the linear model as $\hat{\eta}_i^*$, and the root mean squared error (RMSE) is calculated as the following:

$$RMSE = \sqrt{\sum_{i=1}^N \frac{(\hat{\eta}_{0,i}^* - \bar{\eta}_0^*)^2}{N}}. \quad (14)$$

where $\hat{\eta}_{0,i}^*$ is the predictive viscosity at data point i and N is the total number of the held-out test points.

The sample standard deviation of the test set is calculated as:

$$\sigma = \sqrt{\sum_{i=1}^N \frac{(\eta_{0,i}^* - \bar{\eta}_0^*)^2}{N-1}}. \quad (15)$$

where $\bar{\eta}_0^*$ denotes the mean value of the data in the test set. A typical testing scenario (test/train labeling) is illustrated graphically below (Fig. S10) where the ratio of $\frac{RMSE}{\sigma}$ is found to be 0.36 for η_0^* vs ϕ^* and 0.44 for η_0^* vs ψ^* . This analysis indicates that the linear model fitting of the association between η_0^* and ϕ^* and ψ^* are stronger than random noise.

Table S3: Sensitivity analysis for fitting parameters

Data used	A	β	$\log(C_1)$	$\log(C_2)$
25%	32.1 ± 10.4	3.92 ± 0.86	8.37 ± 1.22	12.1 ± 2.99
50%	33.9 ± 6.24	4.32 ± 0.66	8.88 ± 0.92	12.6 ± 1.77
75%	34.3 ± 5.57	4.43 ± 0.52	9.03 ± 0.73	12.7 ± 1.59
100%	34.1 ± 4.34	4.33 ± 0.45	8.91 ± 0.63	12.7 ± 1.23

(Error bars indicate the 95% confidence interval for the reported values)

Note 6.5 Sensitivity analysis for fitting parameters

The data in the set are rank-ordered by viscosity, from low to high. A total of 35 paired viscosity-composition measurements were used to obtain the parameters for the 100% case, 26 for the 75% case, 17 for the 50% case and 9 for the 25% case.

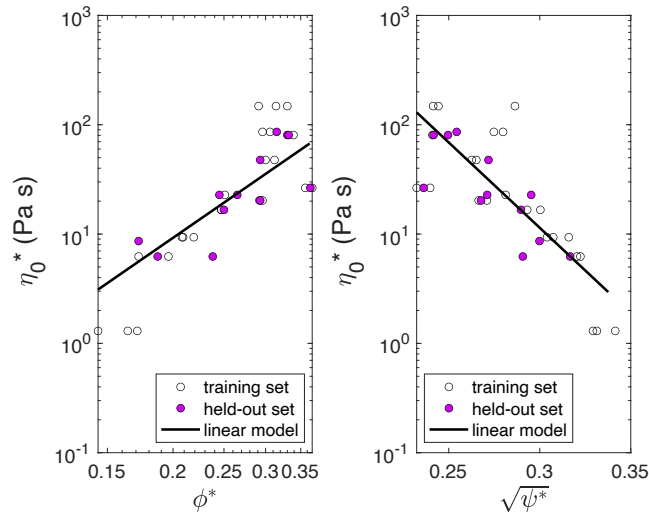


Figure S10: A typical test/train breakdown, where the open circles denote data used for training and filled magenta circles denote data used for testing. The black line denotes the linear model.

Note 6.6 Note on first and second derivatives of the dense phase boundary

Taking the derivatives of Eq. (1) and Eq. (2), we obtain

$$\frac{\partial \psi^*}{\partial \phi^*} = -\frac{2\beta\sqrt{\psi^*}}{A\phi^*}, \quad (16)$$

$$\frac{\partial^2 \psi^*}{\partial (\phi^*)^2} = \frac{2\beta}{A(\phi^*)^2} \left(\frac{\beta}{A} + \sqrt{\psi^*} \right). \quad (17)$$

Because all of the parameters are positive numbers, from Eq. 16 and Eq. 17 we see that the slope of the dense phase boundary is strictly negative while the second derivative of the dense phase boundary is always positive. Hence $\psi^* = f(\phi^*)$ is a decreasing function which is concave (Fig. 6c). This is different from the consensus understanding of the shape of the coacervate phase boundary which is typically convex, and can be attributed to the assumption that A and β are constants in the present analysis. Given that β generally increases with ϕ^* , $\frac{\partial \psi^*}{\partial \phi^*}$ is expected to increase with decreasing salt and increasing polymer concentration, which is exactly what was shown in [5].

References

- [1] James O Berger. *Statistical decision theory and Bayesian analysis*. Springer Science & Business Media, 2013.
- [2] Rungsima Chollakup, Wirasak Smitthipong, Claus D Eisenbach, and Matthew Tirrell. Phase behavior and coacervation of aqueous poly (acrylic acid)- poly (allylamine) solutions. *Macromolecules*, 43(5):2518–2528, 2010.
- [3] Eric M Furst and Todd M Squires. *Microrheology*. Oxford University Press, 2017.
- [4] Jacob N Israelachvili. *Intermolecular and surface forces*. Academic press, 2015.
- [5] Lu Li, Samanvaya Srivastava, Marat Andreev, Amanda B Marciel, Juan J de Pablo, and Matthew V Tirrell. Phase behavior and salt partitioning in polyelectrolyte complex coacervates. *Macromolecules*, 51(8):2988–2995, 2018.
- [6] Alexander Meyer, Andrew Marshall, Brian G Bush, and Eric M Furst. Laser tweezer microrheology of a colloidal suspension. *Journal of rheology*, 50(1):77–92, 2006.